Signal Processing: Image Communication 46 (2016) 17–28

Contents lists available at ScienceDirect

Signal Processing: *Image Communication*

journal homepage: www.elsevier.com/locate/image

A novel framework method for non-blind deconvolution using subspace images priors

Peixian Zhuang, Xueyang Fu, Yue Huang, Delu Zeng, Xinghao Ding *

Fujian Key Laboratory of Sensing and Computing for Smart City, School of Information Science and Engineering, Xiamen University, China

ARTICLE INFO

Article history:
Received 9 November 2015
Received in revised form
14 April 2016
Accepted 14 April 2016
Available online 28 April 2016

Keywords:
Non-blind deconvolution
Subspace images priors
Existing deblurring techniques
Least square integration

ABSTRACT

Non-blind deconvolution has been an active challenge in the research fields of computer vision and computational photography. However, most existing deblurring methods conduct direct deconvolution only on the degraded image and are sensitive to noise. To enhance the performance of non-blind deconvolution, we propose a novel framework method by exploiting different sparse priors of subspace images. In the proposed framework, three effective filters are firstly designed to decompose a degraded image into the measurements of different subspace images. Then, existing deblurring techniques are employed to deblur different blurred subspace images respectively. Finally, the least square integration method is utilized to recover the ideal image by integrating the deblurred estimates of subspace images with the degraded image. The proposed framework is more general and can be easily extended to existing deblurring methods. The conducted experiments have validated the effectiveness of the proposed framework, and have demonstrated that the proposed method outperforms other state-of-the-art methods in both preserving image structures and suppressing noise.

1. Introduction

Image deconvolution has always been an active research area and has attracted considerable attention due to its wide range of applications in computer vision and computational photography [1–3]. The blurry effects are mainly caused by camera shake and object motion while capturing an image. Mathematically, a blurry image can be modeled as

$$y = k \otimes x + \varepsilon \tag{1}$$

where y denotes the blurry image, x is the ideal image, k is the blur kernel, ε is generally assumed to be the white Gaussian noise of zero mean, and $\otimes$ is the 2D convolution operator. The problem of image deblurring can be categorized into two classes of non-blind deconvolution and blind deconvolution. Non-blind deconvolution is to recover the ideal image from the blurry image with the known blur kernel, while blind deconvolution is to restore the ideal image from the blurry image and the unknown blur kernel. Non-blind deconvolution is the main research in this paper. In order to recover the ideal image, prior-enforcing regularizations are used to constrain the optimization problem of image deblurring as

$$\min_x \ell(y, k \otimes x) + \lambda\rho(x) \tag{2}$$

where $\ell(y, k \otimes x)$ measures the data fidelity between $k \otimes x$ and y, $\rho(x)$ denotes the regularization term, and λ is the weight parameter to balance the two terms.

Significant developments on single image deblurring have been witnessed in recent years [4,5]. The pioneering works of image deblurring included the Wiener filter, the Kalman filter, the Tikhonov regularization [6] and the Richardson–Lucy algorithms [7,8]. A well-known total variation (TV) regularization was proposed by Rudin et al. [9,10] for image restoration. The method imposed small penalties on sharp edges and large penalties on smooth regions. The TV regularizations were widely used to recover the ideal image from the degraded image [11,12], but they were still limited by high computational costs due to non-differentiability and non-linearity of the TV functions. A number of fast algorithms have been developed to solve the above limitation. A two-step IST algorithm (TwIST) [13] has been proposed to improve the convergence rate and has achieved better solutions for iterative shrinkage thresholding (IST) [14]. Wang et al. [15] presented fast total variation deconvolution (FTVd) to restore blurry and noisy images using the TV regularization. The algorithm achieved strong convergence and ran orders of magnitude faster than the lagged diffusivity algorithm [16]. Beck et al. [17] derived fast gradient-based algorithms for constrained TV image deblurring problem, and it introduced the monotone version of fast iterative shrinkage thresholding algorithm [18] to achieve faster

* Corresponding author.
E-mail address: dxh@xmu.edu.cn (X. Ding).

http://dx.doi.org/10.1016/j.image.2016.04.003
0923-5965/

convergence rate than the other gradient projections-based methods. Other gradient priors have been effective in approximating the image gradient distributions compared with TV. Krishnan et al. [19] used the hyper-Laplacian priors (HLP) to model gradient distribution of natural images. The method employed an alternating minimization method to solve the non-convex problem and a lookup table method to tackle the per-pixel sub-problem. Krishnan et al. [20] presented an l_1/l_2 regularization scheme for image deblurring, and compensated for the high-frequencies attenuation by adapting l_1 norm regularization with treating the l_2 norm of the image gradients as weights in the iterations. Xu et al. [4,21] took advantage of the l_0 norm of the sparse gradients for image smoothing and deblurring, and this manner controlled the number of non-zero gradients to well approximate image edges and structures. A new l_0-regularized intensity and gradient prior (L0GP) for deblurring text images, proposed by Pan et al. [22], was based on the different statistical properties between the text characters and the background regions. In addition, nonlocal regularization priors have been recently used to recover salient edges and structures by exploiting the nonlocal self-similarity of natural images. A new model of centralized sparse representation (CSR) [23,24] has been proposed to deal with image deblurring. The model exploited the nonlocal self-similarity priors of image patches for sparse coefficients, and minimized the sparse coding noise to improve the performance. Another novel method of joint statistical modeling (JSM) [25] method has been presented by exploiting the local smoothness in the space domain and the nonlocal self-similarity in the transform domain respectively.

Despite the achievements of the above methods, the specific room for their improvements can be manifested as follows: (1) These methods conduct direct deconvolution with the consideration of sparse priors of the whole image, and gradient or nonlocal priors of the ideal image are the key to them. They overlook different priors between subspace images and original images, and do not take account of the difference of subspace images. (2) These methods are sensitive to noise, and are limited in image deblurring as the small amount of noise can be amplified in the deconvolution process. Therefore, we have developed a novel framework method for non-blind deconvolution by exploiting subspace images priors. The main contributions of the paper are given as follows:

- The proposed framework can be generally extended to existing deblurring methods. In this framework, different priors of image subspaces have been utilized to improve the performance of existing methods, and image edges and structures of different subspace images can be differently treated and precisely protected for the performance improvement.
- The proposed approach can be more robust to noise through appropriate decomposition of image subspaces.

The rest of the paper is organized as follows. In Section 2, the previous work of image priors regularization is reviewed. Section 3 describes in detail the motivation and the implementation of the proposed algorithm. The experimental validation of the proposed framework's effectiveness is provided in Section 4. Finally, the conclusion and discussion of the paper is presented in Section 5.

2. Previous work of priors regularization

In recent years, a number of different techniques of prior regularization have been developed for image deblurring. The three well-known classes of the prior regularizations are summarized as follows: (1) Tikhonov regularization [6,15] approximates image priors by Gaussian distributions, and it can be characterized via $|x|_2$. The objective function in this method is quadratic and takes the inexpensive minimization by solving linear systems of equations. (2) Total variation regularizations [9,12] include the two classes of isotropic TV $(\sum_i \sqrt{(\nabla_i^h x)^2 + (\nabla_i^v x)^2})$ and anisotropic TV $(\sum_i |\nabla_i^h x| + |\nabla_i^v x|)$, where ∇_i^h and ∇_i^v denote the first-order horizontal and vertical difference operators, respectively. Since, TV approximations of image priors are more accurate than that of Gaussian distributions, TV regularizations methods achieve better performance than that of Tikhonov. (3) Other priors regularizations [4,19–21] well approximate the distributions of image gradients using hyper-Laplacian norm [19], ℓ_1/ℓ_2 norm [20], and ℓ_0 norm [4,21], which are given as $\sum_i |\nabla_i x|^p$, $(0 < p < 1)$, $\|\nabla x\|_1/\|\nabla x\|_2$ and $\|\nabla x\|_0$, respectively. The deblurring results can be further improved because the approximation representations of prior distributions are more accurate. It is manifested that more accurate priors will bring in more performance improvements.

It is observed that the closed-form solution to the above mentioned deblurring methods can be summarized as the frequency-domain weighted operations, and the specific expression can be generally written as

$$x = F^{-1}\left\{\frac{F^*(k) \odot F(y) + \sum_i \lambda_i F^*(D_i) \odot F(\beta_i)}{F^*(k) \odot F(k) + \sum_i \lambda_i F^*(D_i) \odot F(D_i)}\right\} \tag{3}$$

where F and F^* are the Fourier transform and its complex conjugate operation, respectively; F^{-1} is the inverse Fourier transform; $\odot$ denotes the element-wise multiplication operator; $\{\lambda_i\}$ are regularization parameters to balance the above terms; $\{\beta_i\}$ are the latent estimates of an image or a gradient-domain image, which are derived based on the corresponding priors; and D_i is the operator of prior extraction. When D_i is the identity matrix, Eq. (3) will be degraded into the solution to the Tikhonov regularization methods [6,15]. The employment of this over-smoothed regularization produces unclear image edges and structures. When D_i denotes the first-order difference operators (e.g., $[1, -1]$ and $[1; -1]$), Eq. (3) will be the solution of the well-known methods based on the gradient-domain priors (TV and other priors regularizations). These approaches perform the weighted operations between the degraded image and the image gradient priors, and overcome the problem of blurred edges and structures by employing more accurate priors. However, it is observed that the entire denominator of the solution in the frequency domain (below shown in Fig. 3(c) and (d)) contains zero values and small values close to zero, which easily cause noise amplification results in image deblurring process.

3. The motivation and design of the proposed framework

3.1. Motivation

A divide-and-conquer scheme is proposed for non-blind deconvolution using subspace decomposition. The motivation of image subspaces decomposition is presented from two viewpoints, priors difference and model errors difference. Both are analyzed in detail as follows: (1) *Priors difference*: The priors of image gradient have been successfully employed for image deblurring in previous works, and more accurate priors improve deblurring performances. However, existing deblurring methods only utilize the whole sparse prior from an entire image, and overlook the difference between subspace images. Fig. 1(a) and (b) show the gradient distributions of the original and the subspace images of image Lena, meanwhile, Fig. 1(c) and (d) show the average gradient distributions of 100 images (Google image dataset shown in Section 4) for the original and the subspace images. From Fig. 1, it can be clearly seen that the gradient distributions of

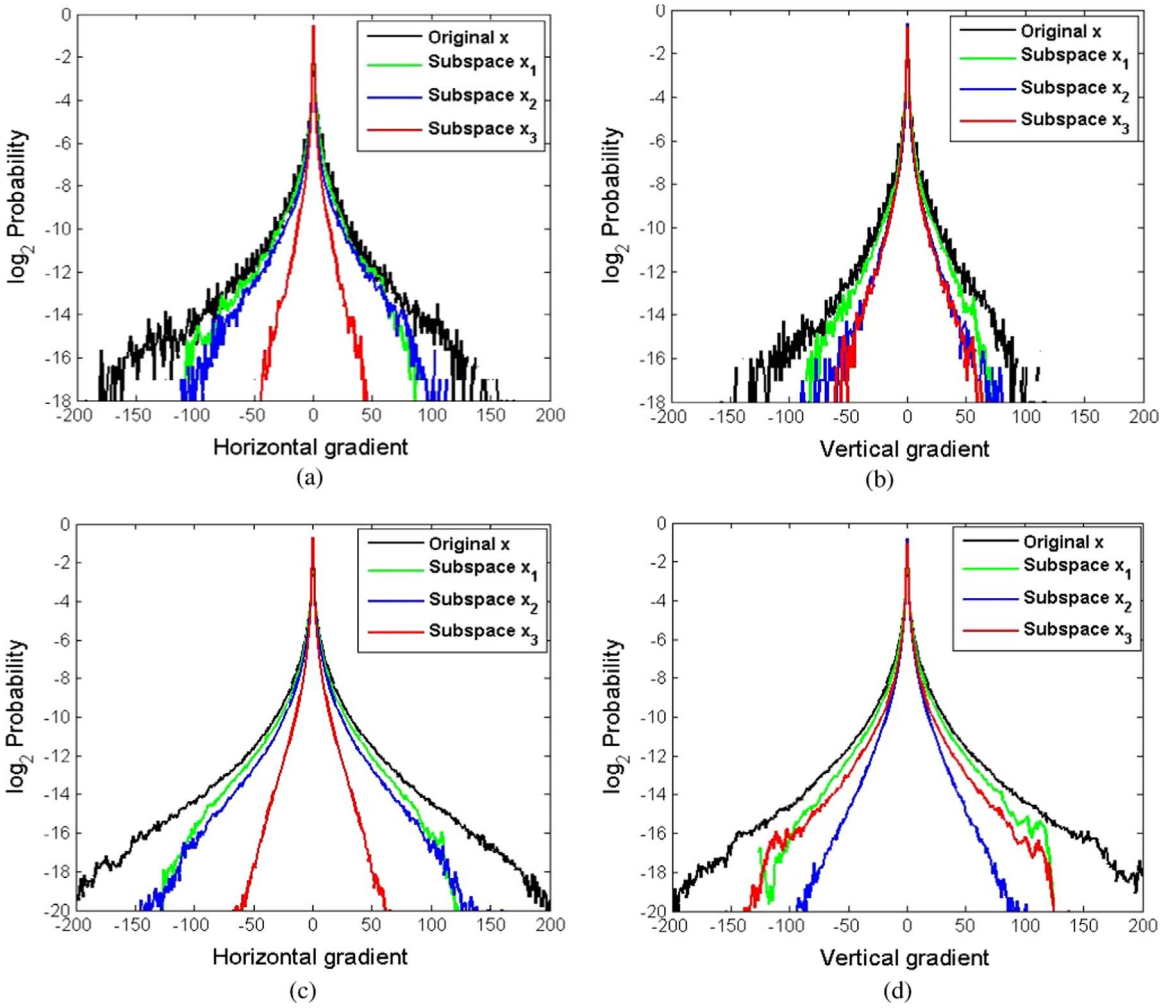

Fig. 1. Gradient distributions of the original and the subspace images. (a) and (b) gradient distributions of four kinds of images (original image x (black), subspace $x_1 = h_1 \otimes x$ (green), subspace $x_2 = h_2 \otimes x$ (blue) and subspace $x_3 = h_3 \otimes x$ (red). where $\{h_i\}_{i=1}^3$ are given below formula (10)) on image Lena. (c) and (d) average gradient distributions of four kinds of images on the 100 images (Google image dataset in Section 4). X -axis: gradient values, and Y -axis: probability values in log 2 domain. (For interpretation of the references to color in this figure caption, the reader is referred to the web version of this paper.)

the subspace images are obviously different from that of the original image, and gradient distributions of different subspace images are clearly different. Therefore, precise consideration and accurate exploitation of different priors in subspace images can further improve the deblurring performance. (2) *Model errors difference*: The existing methods measure the model errors based on the assumption that all image pixels are equally important for image recovery. However, it has been found that image edges and structures are more important than smooth areas of the image for image restoration [29,23,24], and image high-frequency components are more significant than that of low-frequency due to the fact that image edges and structures are mainly concentrated in image high-frequency components. It is necessary to take the difference between smooth areas and image edges and structures into consideration, and to differently and precisely protect image edges and structures in different subspaces of the image for the performance improvement. Different from the traditional model as Eq. (1), we analyze the degraded model of the i-th subspace image based on the below Eq. (6) as follows:

$$y_i = k \otimes x_i + \varepsilon_i = k \otimes (\hat{x}_i + \Delta\hat{x}_i) + \varepsilon_i = k \otimes \hat{x}_i + \underbrace{k \otimes \Delta\hat{x}_i}_{\varepsilon_e} + \varepsilon_i$$

$$= k \otimes \hat{x}_i + \varepsilon_e + \varepsilon_i \tag{4}$$

where $\hat{x}_i$ is the estimate of x_i, $\Delta\hat{x}_i = x_i - \hat{x}_i$, ε_e denotes the model noise, ε_i is the measurement noise assumed to be the Gaussian distribution of zero mean, x_i and y_i are the i-th subspace images of x and y, respectively. In Eq. (4), it can be found that the existing methods easily mistake the model noise as one part of the measurement noise. However, the model noise including image edges and structures is significantly different from the measurement noise. Fig. 2 shows the model errors (namely, $e = y - k \otimes \hat{x}$ and $e_i = y_i - k \otimes \hat{x}_i = \varepsilon_e + \varepsilon_i$, where the original estimate $\hat{x}$ and the subspace estimate $\hat{x}_i$ are obtained using the same deblurring methods. $i = 1, 2, 3$) distributions of the original and the subspace images by FTVd [15] and HLP [19], respectively. The model errors distributions of image Lena by the above mentioned methods are shown in Fig. 2(a) and (c), and the average distributions of model errors of the 100 images (Google image dataset in the Section 4) are shown in Fig. 2(b) and (d). It can be observed that the model errors distributions of the subspace images are different from that of the original image, meanwhile, different subspace images have different distributions of model errors. It is manifested that the model errors of different subspace images have different relative accuracy for the reconstruction of image edges and structures, and the better deblurring methods can yield better recovery of image edges and structures. Therefore, different treatment and precise protection of image edges and structures of different subspace

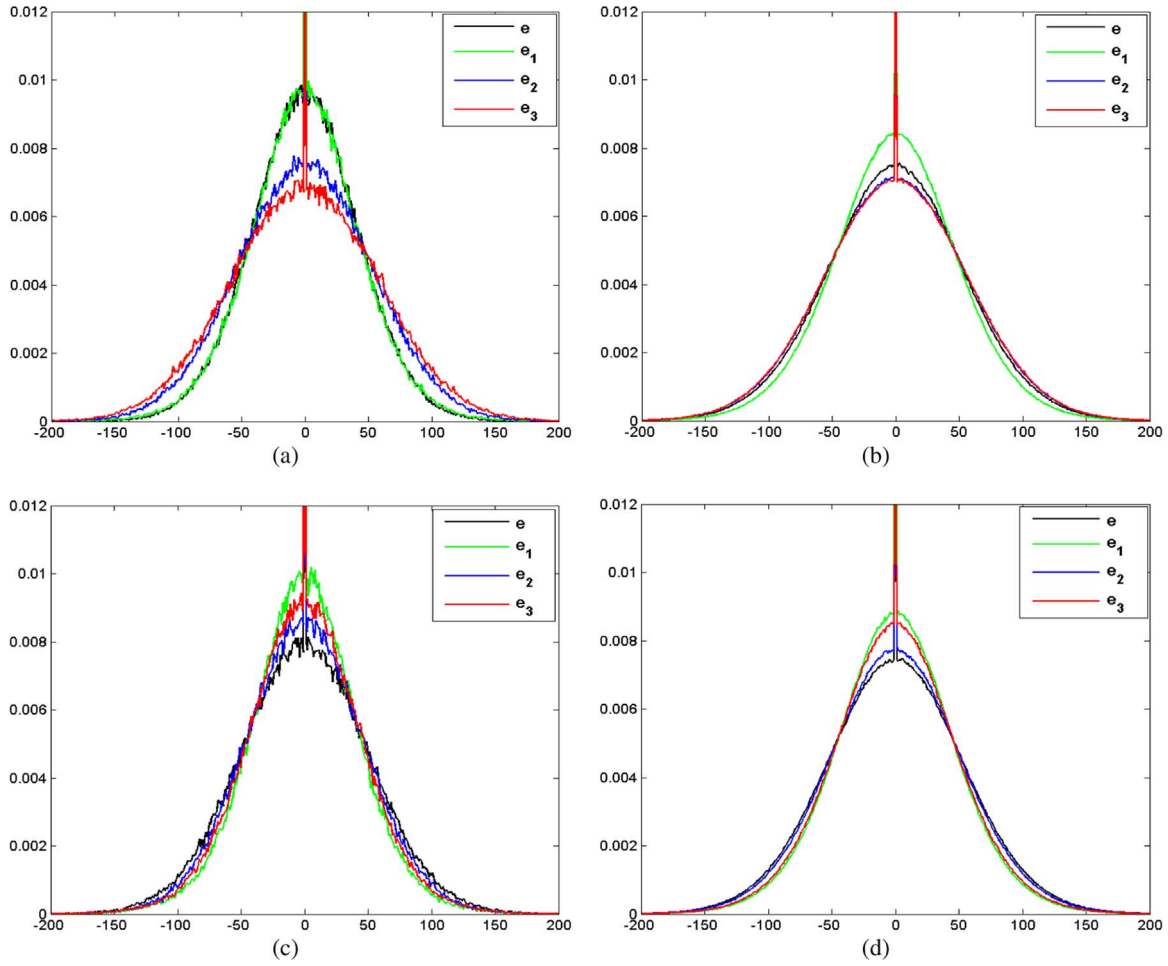

Fig. 2. Model errors distributions of the original and the subspace images. (a) and (c) Model errors distributions of image Lena by FTVd [15] and HLP [19], respectively. (b) and (d) Average model errors distributions of the 100 images (Google image dataset in Section 4) by FTVd [15] and HLP [19], respectively.

images can also enhance the performance.

In addition, existing deblurring methods are sensitive to noise. It is observed from Eq. (3), that the denominator of the solution will produce the zero-holes effect (zero values and small values close to zero in the frequency domain) when the blur kernel and the prior operators will not be able to completely fill the entire frequency domain. Specifically, the values of $F(D_i)$ (e.g., D_i as image gradient priors) are generally concentrated in the periphery of the frequency domain (Fig. 3(d)), while the most elements of $F(k)$ (e.g., k as the blur kernel) are mainly concentrated in the center of the frequency domain (Fig. 3(c)), when the blur degree is high, and it leads to zero values and some values close to zero in the middle region. If the noise is present in the blurry image, the zero-holes effect will lead to the amplified periodic noise (Fig. 3(b)) in the deblurred image. This is the main reason for the noise sensitivity of the above deblurring methods. Therefore, it is necessary to consider the ability of prior operators to solve the problem of zero-holes effect by designing corresponding operators.

3.2. The proposed framework

The following notation will be used in this section: S is the total number of subspace images. $\{x_i \in R^{N\times N}\}_{i=1}^{S}$ are S subspace images of the ideal image x, $\{X_i \in C^{N\times N}\}_{i=1}^{S}$ are the Fourier transforms of corresponding subspace images, $\{\hat{x}_i\}_{i=1}^{S}$ are the corresponding estimates of $\{x_i\}_{i=1}^{S}$, and $\{\hat{X}_i\}_{i=1}^{S}$ are the Fourier transform estimates of $\{\hat{x}_i\}_{i=1}^{S}$. $\{y_i \in R^{N\times N}\}_{i=1}^{S}$ denote S blurred observations of the ideal subspace images $\{x_i\}_{i=1}^{S}$. $\{h_i\}_{i=1}^{S}$ are defined as S linear filters, $\{H_i\}_{i=1}^{S}$ are corresponding frequency responses, and $\{H_i^*\}_{i=1}^{S}$ are the complex conjugate of $\{H_i\}_{i=1}^{S}$. Y is the Fourier transform of the degraded image y. K and K^* are the Fourier transform and its complex conjugate of the blur kernel k, respectively. $\mathbf{1}$ is a matrix in which every element is equal to one.

Based on the theory of signal decomposition in linear systems [28], image subspaces decomposition can be fulfilled by the group of linear filters. Hence, the i-th subspace image x_i of the ideal image x can be expressed as

$$x_i = h_i \otimes x \tag{5}$$

Similarly, based on the commutative property of linear systems [28], and using the formulations (1) and (5), the i-th blurred subspace image y_i can be derived as follows:

$$y_i = h_i \otimes y \overset{(1)}{=} h_i \otimes \underbrace{(k \otimes x + \varepsilon)}_{y} = k \otimes \underbrace{(h_i \otimes x)}_{x_i} + \underbrace{h_i \otimes \varepsilon}_{\varepsilon_i}$$
$$\overset{(5)}{=} k \otimes x_i + \varepsilon_i \tag{6}$$

It is found from Eq. (6) that the blurred subspace images $\{y_i\}_{i=1}^{S}$ are the corresponding observations of the ideal subspace images $\{x_i\}_{i=1}^{S}$, and $\{y_i\}_{i=1}^{S}$ can be obtained by directly employing the linear filter group $\{h_i\}_{i=1}^{S}$ to convolve the degraded image y.

Once the blurred subspace images are obtained, the advantage of different priors from different subspace images is taken into account, and one of existing deblurring methods is used to deblur

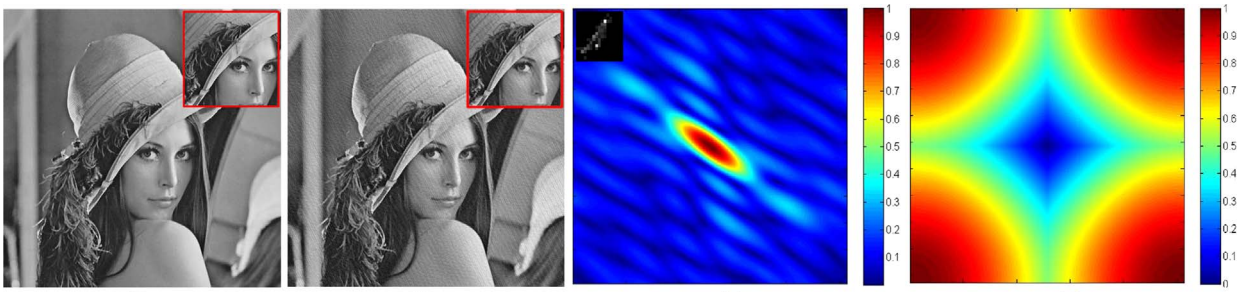

Fig. 3. Zero-holes effect of image Lena by HLP [19]. (a) and (b) are the deblurred results of HLP [19] without and with Gaussian noise (standard deviation: 0.76), respectively. (c) and (d) are the Fourier-domain spectrum diagrams of $F^*(k) \odot F(k)$ and $\sum_{i=1}^{2} F^*(D_i) \odot F(D_i)$ of Eq. (3), respectively. $D_1 = [1, -1]$ and $D_2 = [1; -1]$. The blur kernel is shown at the top left corner of (c).

the blurred subspace images respectively. Thus the deblurred estimates of subspace images $\{\hat{x}_i\}_{i=1}^{S}$ are achieved by deblurring different blurred subspace images $\{y_i\}_{i=1}^{S}$. It should be noted that the conventional problem of image deblurring is converted into the sub-problems of deblurring different subspace images. The detailed sub-problem is formulated as

$$\hat{x}_i = \arg\min_{x_i} \frac{1}{2} \| y_i - k \otimes x_i \|^2 + \eta_i \rho(x_i) \tag{7}$$

where $\rho(x_i)$ denotes the prior regularization term, and $\{\eta_i\}_{i=1}^{S}$ are the parameters to balance the above two terms. Figs. 1 and 2 demonstrate that the prior distributions of different subspace images are different, and the model error distributions of different subspace images are different. Therefore, based on the rule of maximum a posteriori (MAP), different parameters are adopted to better balance the prior term and the model error term for image subspaces deblurring.

Aftering obtaining the deblurred estimates of subspace images $\{\hat{x}_i\}_{i=1}^{S}$, and meeting the constraint conditions of the formulations (1) and (5), the final formulation of the objective function is written as

$$\hat{x} = \arg\min_{x} \frac{1}{2} \| y - k \otimes x \|^2 + \frac{1}{2} \sum_{i=1}^{S} \lambda_i \| \hat{x}_i - h_i \otimes x \|^2 \tag{8}$$

where $\{\lambda_i\}_{i=1}^{S}$ are the weighting parameters to balance the above terms. The model error term $\frac{1}{2} \| y - k \otimes x \|^2$ ensures the global similarity of the image, and integrates the degraded image to compensate the information loss of subspace images recovery. The regularization terms $\frac{1}{2} \sum_{i=1}^{3} \lambda_i \| \hat{x}_i - h_i \otimes x \|^2$ satisfy the constraint relations between the ideal image x and the estimates of ideal subspace images $\{\hat{x}_i\}_{i=1}^{3}$, which are based on Eq. (5). Finally, the method of least square integration [29] is employed to solve the problem (8), and fast Fourier transform [30] is used to speed up the convolution operations. The final closed-form solution $\hat{x}$ can be derived as

$$\hat{x} = F^{-1}\left\{ \frac{K^* \odot Y + \sum_{i=1}^{S} \lambda_i H_i^* \odot \hat{X}_i}{K^* \odot K + \sum_{i=1}^{S} \lambda_i H_i^* \odot H_i} \right\} \tag{9}$$

Effective linear filters are designed to decompose the entire image into different subspace images. The detailed forms of linear filters are given below:

$$\begin{cases} h_1 = [0.5; 0.5] \otimes [0.5, 0.5] \\ h_2 = [-0.5, 0.5] \\ h_3 = [-0.5; 0.5] \otimes [0.5, 0.5] \end{cases} \tag{10}$$

where [0.5,0.5] and [0.5;0.5] are the horizontal and vertical low-pass filters, respectively; [−0.5,0.5] and [−0.5;0.5] are the horizontal and vertical high-pass filters, respectively. Three filters $\{h_i\}_{i=1}^{3}$ are determined based on the following aspects: (1) The filters must ensure the completeness of entire image decomposition, and the formulation of filters completeness in the Fourier domain is written as

$$\sum_{i=1}^{3} H_i = \mathbf{1} \tag{11}$$

Based on the definition of the filters, another significant completeness of the filters in the Fourier domain can be derived as

$$\sum_{i=1}^{3} H_i^* \odot H_i = \mathbf{1} \tag{12}$$

The detailed proof of Eq. (12) can be seen in Appendix A. From Eq. (9), it can be observed that the denominator of the final solution contains the terms $\sum_{i=1}^{3} \lambda_i H_i^* \odot H_i$, and we can take manually tuned weights $\{\lambda_i\}_{i=1}^{3} > 0$) and utilize the above filters completeness (Eq. (12)) to get the entire denominator to be nonzero values away from zero values and small values close to zero, which can avoid noise amplification caused by the zero-holes effect (when many elements of $K^* \odot K$ are zero values and small values close to zero in the frequency domain). (2) The filters decompose the entire image into different subspace images, and facilitate to precisely exploit both different priors from subspace images and differently protect image edges and structures in the model errors of different subspace images for better recovery of the ideal image. (3) The effectiveness of the proposed decomposition with three filters is experimentally validated for the performance improvement (comparison of different subspaces decomposition methods in Section 4.4). Based on meeting the above mentioned completeness of image subspaces decomposition, the proposed framework with three filters' decomposition can save the operation time, and can achieve better performance than that of other decomposition methods.

The overview of the proposed method is shown in Fig. 4. The three main steps of the proposed framework are sketched in Algorithm 1.

Algorithm 1. Outline of the proposed framework.

Input: Blurred image y , kernel k , balancing weights $\{\lambda_i\}_{i=1}^{3}$

Output: Deblurred image $\hat{x}$

1: Obtain blurred subspace images $\{y_i\}_{i=1}^{3}$ via Eq. (6).

2: Achieve the deblurred estimates of subspace images $\{\hat{x}_i\}_{i=1}^{3}$ by employing one of existing deblurring methods to deblur $\{y_i\}_{i=1}^{3}$ respectively.

3: Solve for $\hat{x}$ via Eq. (9).

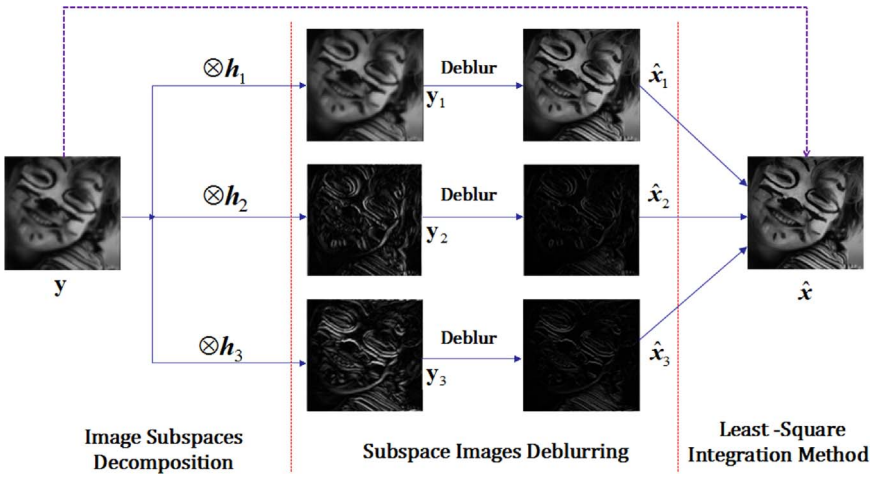

Fig. 4. Overview of the proposed framework.

4. Experiment validation

In this section, the effectiveness of the proposed framework algorithm has been validated through numerous experiments and the results have been compared with other state-of-the-art methods (TwIST [13], L0GP [22], FTVd [15], JSM [25] and HLP [19]). All the experiments have been conducted in Matlab 2012a on a SAMA computer with Intel CPU E3-1230 v3 processor (3.3 GHz) and 16 GB Memory. In the implementation, the peak signal-to-noise ratio (PSNR) and improvement in signal-to-noise ratio (ISNR) [31] are measured as the quantitative evaluations. The visual quality of deblurred images is taken as the qualitative evaluation. Different parameters of the same method are applied to different subspace images deblurring, however, these parameters have certain universality and are fixed for all test images. All weighting parameters are manually tuned for the best PSNR and ISNR improvements. The proposed framework is compared with TwIST [13], L0GP [22], FTVd [15], JSM [25] and HLP [19] on extended Levin dataset [32], Google image dataset and general blurs on the classic images, respectively. The extended Levin dataset consists of 4 base images (the first four images in Fig. 5) with size of 255×255 and 10 blur kernels. 8 kernels are from Levin dataset, and other 2 kernels are from [19]. We build a Google image dataset containing 100 images from which 4 representative images are the middle four images in Fig. 5. Classical test images of Cameraman, Lena and Barbara are the last three images in Fig. 5. The general blurs contain four blur kernels: a 11×11 uniform kernel, a Gaussian kernel using fspecial ('Gaussian',25,10), a motion blur kernel using fspecial ('Gaussian',15,45), and a 25×25 average kernel. The deblurring performance of different methods is compared on image Barbara with Gaussian noise of different levels. The method of Zhong [27] is employed for comparing the noise-aware deblurring performance of the proposed framework. Finally, different ways of image subspaces decomposition and different methods of image subspaces integration are compared to validate the effectiveness of the proposed framework, respectively.

4.1. Extended Levin and Google image dataset comparison

We perform the evaluation on the benchmark dataset of extended Levin. The average PSNR and average ISNR of 4 base images (Im05, Im06, Im07 and Im08) are shown in Fig. 6. Each image is blurred with 10 different kernels and is noised with the same standard deviation of Gaussian noise. Fig. 6 demonstrates that the proposed framework of subspaces decomposition can be extended to other deblurring methods, and the proposed framework methods have achieved both average PSNR and average ISNR higher than the original methods of TwIST [13], L0GP [22], FTVd [15], JSM [25] and HLP [19], respectively. The overall performance improvements are mainly attributed to precise utilization of different priors of image subspaces and distinguish the proposed method from previous methods which only consider the priors of image itself. Least improvements have been achieved on the deblurring performance of TwIST [13] due to the limitations of initializations and TV models. Although, gradient distributions of the entire image have been well approximated by hyper-Laplacian

Fig. 5. Original test images.

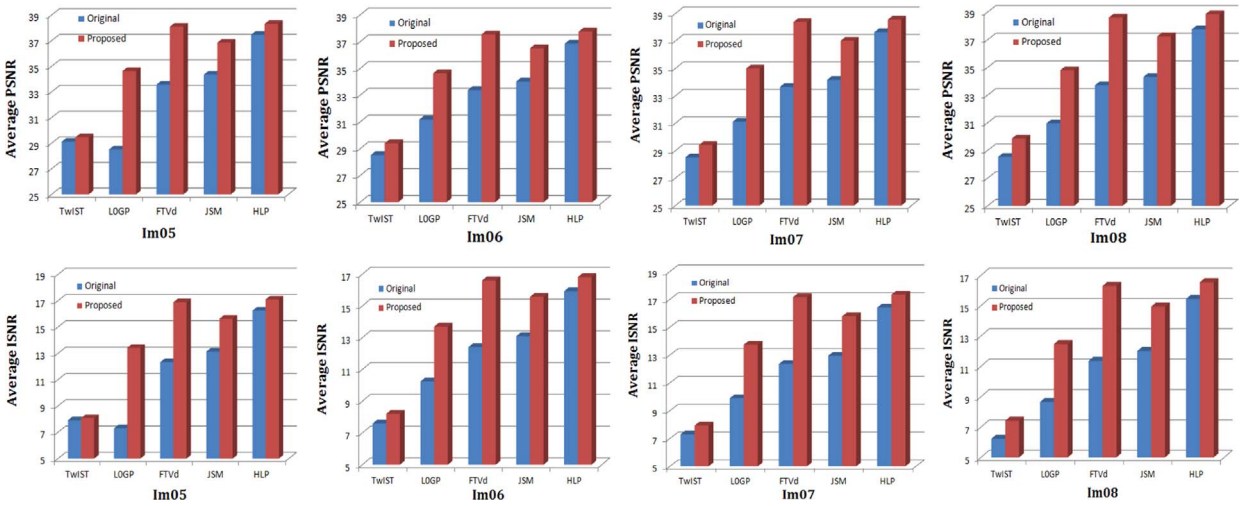

Fig. 6. Comparison of different methods on extended Levin dataset. Blue columns: original methods of TwIST, L0GP, FTVd, JSM, HLP, respectively. Red columns: the proposed framework methods based on these five methods. (For interpretation of the references to color in this figure caption, the reader is referred to the web version of this paper.)

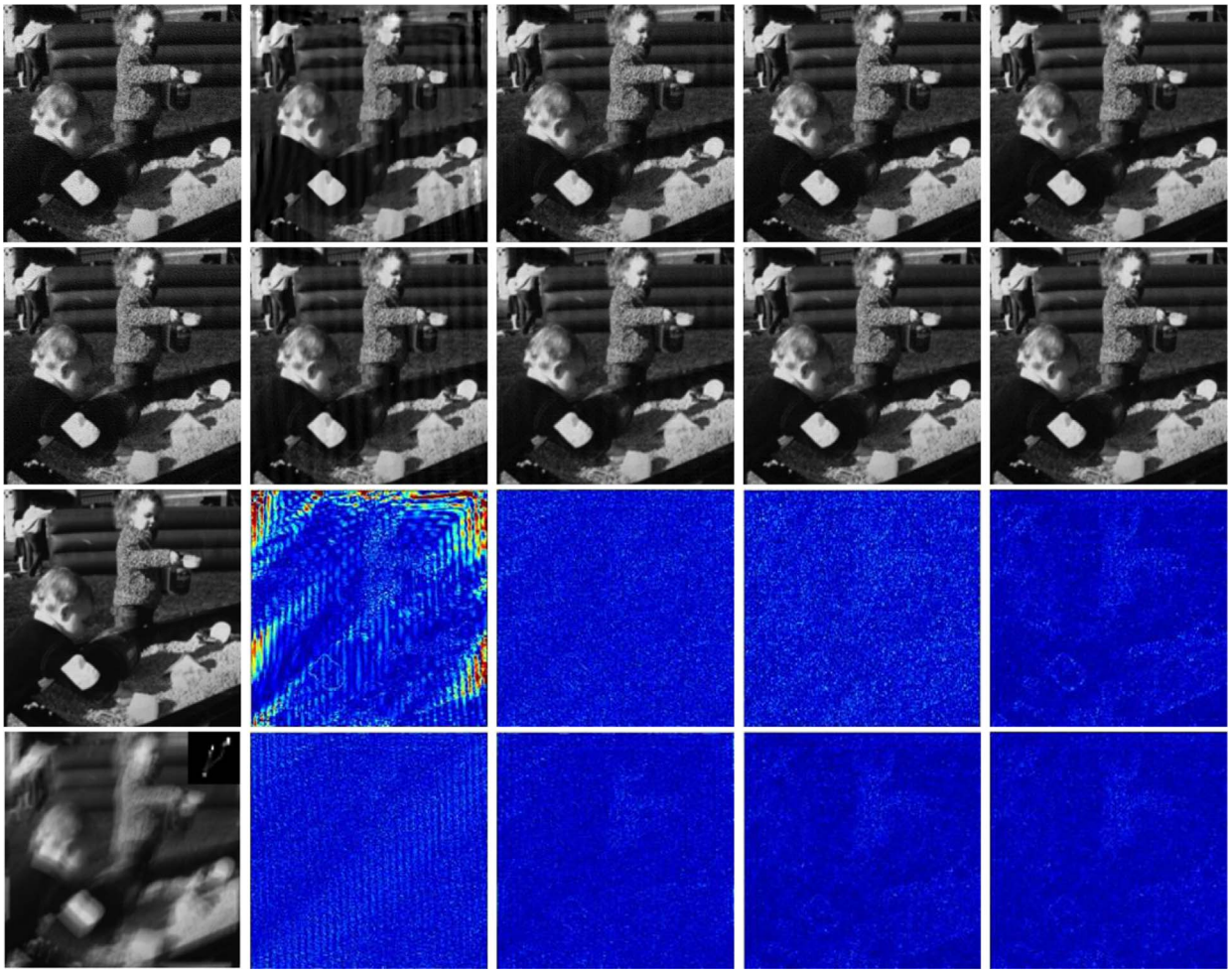

Fig. 7. The deblurring results on the Im05 blurred with the kernel 8. Row 1: TwIST, L0GP, JSM, FTVd and HLP, respectively. Row 2: Proposed framework based TwIST, L0GP, JSM, FTVd and HLP, respectively. Row 3: original image, absolute errors of L0GP, JSM, FTVd, HLP, respectively. Row 4: blur image and the kernel, absolute errors of proposed methods based L0GP, JSM, FTVd, HLP, respectively.

distributions but the deblurring performance can be still improved for HLP [19] by employing the priors from other subspaces. The proposed methods have achieved large improvements both on average PSNR and average ISNR for L0GP [22], FTVd [15] and JSM [25], respectively. They are attributed to the utilization of different priors of image subspaces, in addition to the priors of image intensity for L0GP [22], the warm-start parameters for FTVd [15], and image nonlocal self-similarity for JSM [25], respectively. Fig. 7 shows the deblurring results and residual errors (in absolute value) of different methods on the Im05 blurred with the kernel 8.

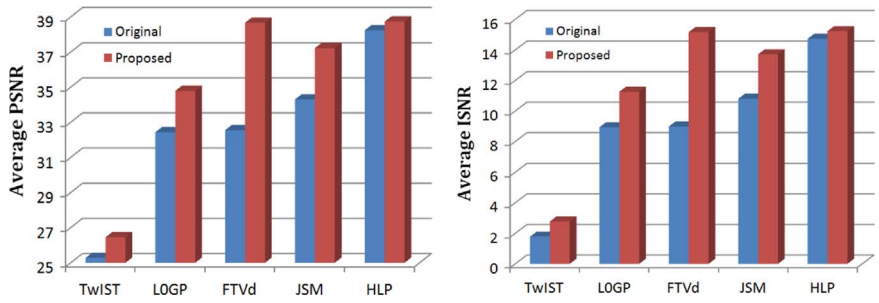

Fig. 8. Performance comparison of different methods on Google image dataset.

The residual errors of TwIST [13] versus proposed are not given due to space limitation. The deblurred result of TwIST [13] has some residual noises, which are generated from the limitations of the initialization and TV regularizations. L0GP [22] has produced the worse results of serious strip artifacts caused by introducing the non-sparse prior of image intensity. JSM [25] has slightly weak artifacts in the deblurred image with the remedy of using nonlocal self-similarity of image patches. FTVd [15] and HLP [19] achieve better results but small residual noises. However, by considering different priors of image subspaces and designing effective filters, the methods in the proposed framework can both preserve detail structures and suppress noise better than the original methods of TwIST [13], L0GP [22], FTVd [15], JSM [25] and HLP [19]. In addition, different deblurring methods have been compared on Google image dataset, which contains 100 images blurred with the kernel 8 and noised with the same standard deviation of Gaussian noise. The average values of PSNR and ISNR are computed in Fig. 8. It can be observed that proposed framework methods have achieved highest values in all cases, which validates the effectiveness of the proposed framework.

4.2. General blurs comparison

In case of general blurs, the test images of Cameraman and Lena are blurred by a blur kernel (chosen one from above four blur kernels) and then noised by the same standard deviation of Gaussian noise. The average PSNR and ISNR values of different methods are shown in Fig. 9, where it can be seen that the proposed approaches are still outperforming other methods of TwIST [13], L0GP [22], FTVd [15], JSM [25] and HLP [19] in deblurring performance. The visual comparisons of different deblurring methods are shown in Fig. 10. The residual errors of TwIST [13] versus proposed are not given due to space limitation. The result of TwIST [13] has some residual noise, and the results of L0GP [22] and JSM [25] have some serious artifacts. FTVd [15] and HLP [19] have achieved relatively better results but have lost detail structures. The reasons for the low performance of all above methods are the same as described in Section 4.1. However, it is observed that the proposed framework methods have achieved better performance compared to other methods in terms of noise reduction, artifacts suppression and detail structures preservation. The higher performance of the proposed methods can benefit from utilizing precise priors of image subspaces and designing effective filters to suppress noise.

4.3. Deblurring performance with noise

Experiments have been performed to explore the noise effect on the proposed and other methods in image deblurring. Fig. 11 shows the PSNR and ISNR curves of different methods on image Barbara, which is blurred with the kernel 5 and corrupted with different levels of Gaussian noise. The PSNR and ISNR plots of the proposed methods are higher than that of the above five original methods with different noise levels. It is demonstrated that the proposed methods have achieved better deblurring performance and noise robustness in comparison. In addition, the comparison with the noise-robust deblurring method of Zhong [27] is performed. Fig. 12 shows the PSNR and ISNR curves of the proposed and Zhong [27] methods on images Barbara and Cameraman, which are both blurred with the kernel 10 and noised with the Gaussian noise of different levels. The PSNR and ISNR plots of the proposed method are mostly higher than that of Zhong. It is admitted that the Zhong [27] method outperforms the proposed method in the case of large noise levels, however, the former fails in low and medium noise levels caused by information loss during its two-step process [26,33]. Therefore, it is observed that the proposed method achieves better performance than Zhong when noise levels are within a certain range. The deblurred results of proposed and Zhong [27] methods are shown in Fig. 13, where it can be seen that the proposed method outperforms the method of Zhong on artifacts suppression and detail structures protection. Table 1 shows PSNR and ISNR variance of different methods in noise variation (noise levels as same as Figs. 11 and 12) respectively. It can be seen that the PSNR and ISNR variance values of proposed methods are comparable or smaller than that of TwIST [13], HLP [19], FTVd [15] and JSM [25]. L0GP [22] and Zhong [27] achieve consistent poor performances in most cases of noise variation, which leads to smaller PSNR and ISNR variances.

4.4. Comparison of different subspaces decomposition

In this subsection, the proposed decomposition with other methods of image subspaces decomposition (namely, two subspaces decomposition with two empirical filters $[1,-1]$ and

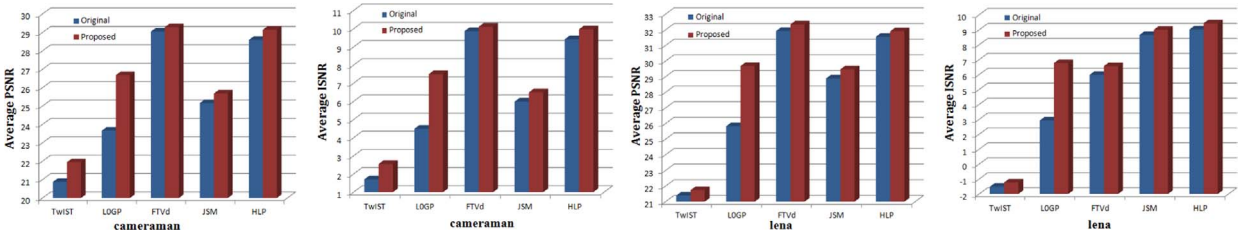

Fig. 9. Performance comparison of different methods on general blurs.

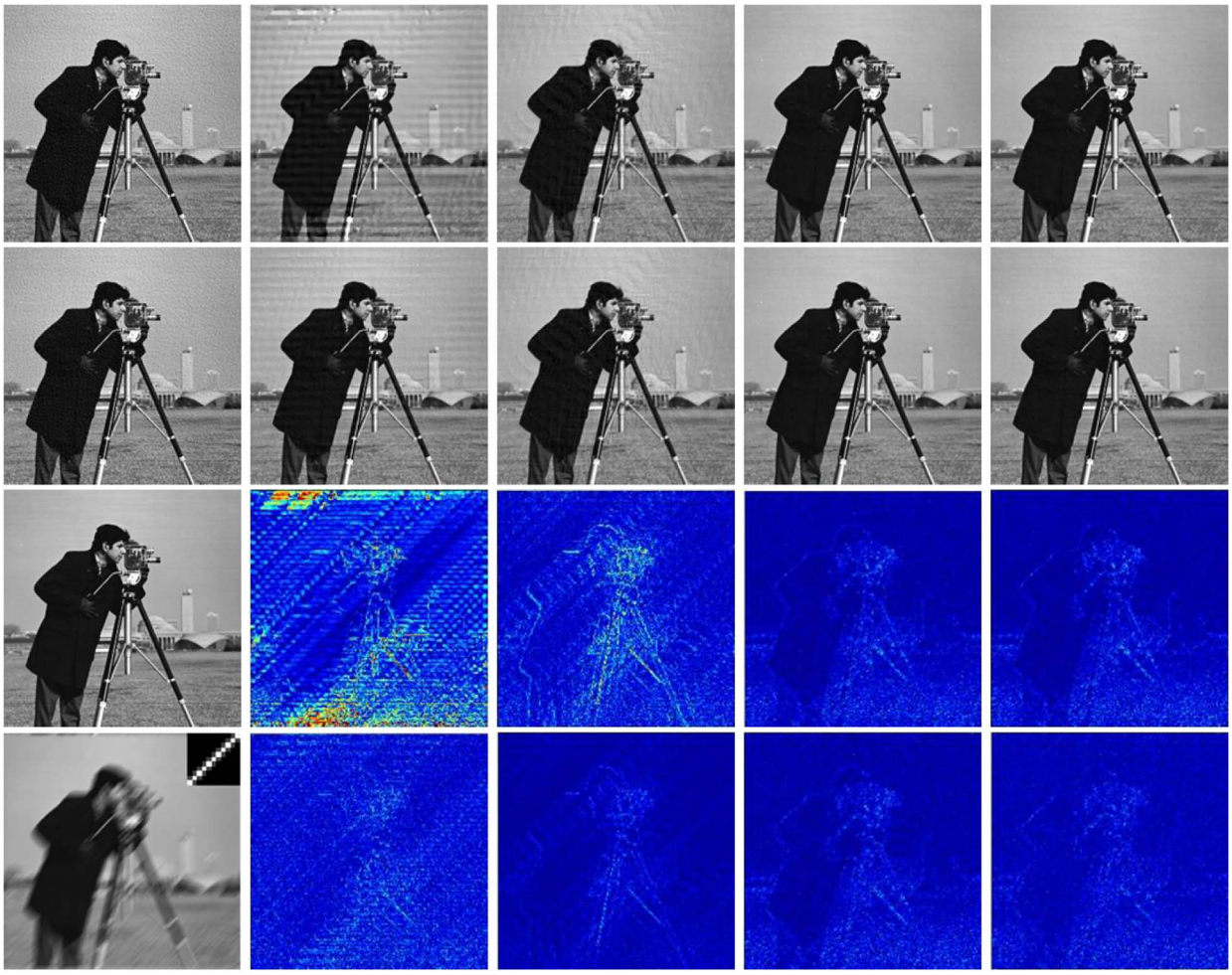

Fig. 10. The deblurring results of Cameraman with motion blur kernel. Row 1: TwIST, L0GP, JSM, FTVd and HLP, respectively. Row 2: the proposed framework based TwIST, L0GP, JSM, FTVd and HLP, respectively. Row 3: original image, absolute errors of L0GP, JSM, FTVd, HLP, respectively. Row 4: blur image and the kernel, absolute errors of proposed framework based L0GP, JSM, FTVd, HLP, respectively.

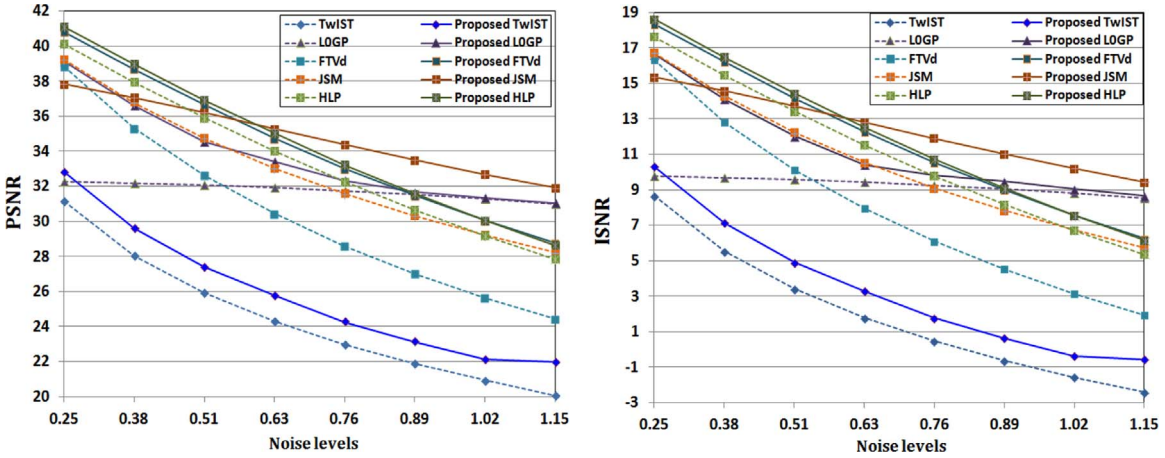

Fig. 11. Comparison of different methods in different noise levels. X-axis: standard deviation of Gaussian noise, Y -axis : PSNR and ISNR.

[1; −1]; four subspace decomposition with four filters [0.5, 0.5], [−0.5, 0.5], [0.5; 0.5] and [−0.5; 0.5]) is compared in image deblurring. Fig. 14 shows the performance comparison of FTVd [15] with different ways of subspace decomposition (the original FTVd, proposed FTVd with two subspaces decomposition, proposed FTVd with four subspaces decomposition, and the proposed FTVd) on Im08. It can be seen that the proposed method has achieved average PSNR and average ISNR higher than other methods (the original FTVd, proposed FTVd with two and four subspaces decomposition, respectively). As illustrated in Fig. 3 and described in Section 3.1, the deblurring method with two empirical filters cannot tackle the problem of noise amplification in image deblurring caused by zero values and small values close to zero in the frequency domain. Both the proposed decomposition and the proposed framework with four subspaces decomposition can solve the mentioned problem by simultaneously exploiting the

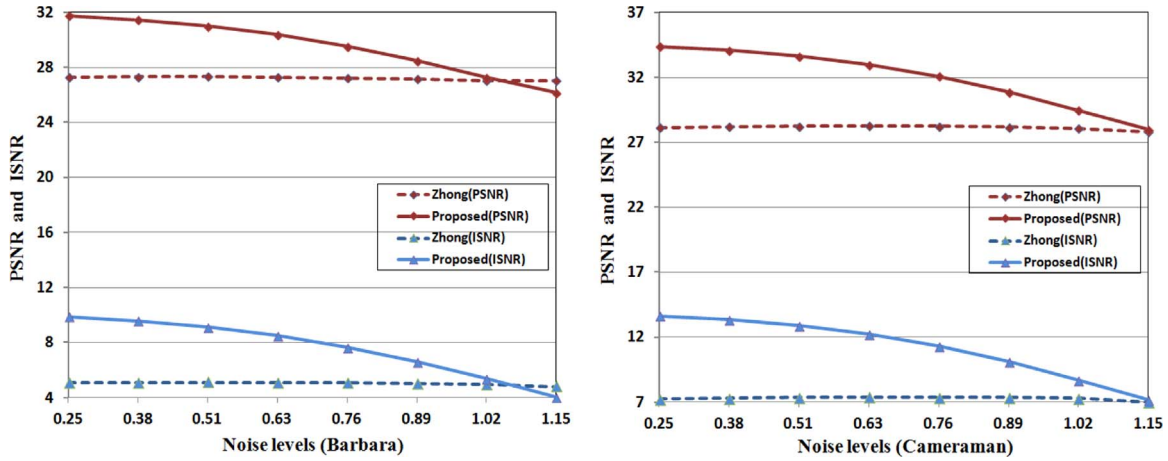

Fig. 12. Comparison of proposed and Zhong [27] methods in different noise levels. *X* -axis: standard deviation of Gaussian noise, *Y* -axis : PSNR and ISNR.

completeness of designed filters and manually adjusting corresponding weights. However, compared with four subspaces decomposition, the proposed decomposition with three subspaces can shorten the operation time and achieve tremendous performance improvements.

4.5. Comparison of different integration methods

In the final subsection, the comparison of different methods of image subspaces integration is performed to validate the effectiveness of the proposed framework with least-square integration. From Fig. 15, it can be clearly observed that the proposed framework with the least-square integration method (Eq. (9)) outperforms the original and the proposed with the sum integration method ($\hat{x} = \sum_{i=1}^{3} \hat{x}_i$) in the performance of PSNR and ISNR. The performance improvement benefits from integrating the degraded image to compensate the information loss of subspace images recovery. Compared with the sum integration method, the least-square integration method introduce more weighting parameters to balance the terms of Eq. (8), but these parameters have certain universality and are fixed for all test images. It is demonstrated that the least-square integration method can be effective for image subspaces integration.

5. Conclusion and discussion

In this presented work, a novel framework based on subspace images priors has been developed for non-blind deconvolution. To utilize different priors of subspace images and to tackle noise amplification, we have designed effective filters to divide the entire image into different subspace images, and then have used the previous techniques to deblur these blurred subspace images respectively. In the final step, the least square integration method has been employed to restore the ideal image from integrating deblurred subspace images with the degraded image. The proposed framework can be effectively extended to other existing methods, and the experimental simulations have demonstrated the effectiveness of proposed framework on deblurring performance and noise robustness. The limitation of the proposed method is that subspace images deconvolution takes more time than the existing methods only deblurring on the degraded image. Table 2 shows the average time consumption comparison of different methods of TwIST [13], L0GP [22], FTVd [15], JSM [25] and HLP [19] on Google image dataset (the 100 images in Section 4). As can be seen, the proposed methods take about two or less than three times than the above original methods. However, the parallel computation by GPU hardware can be adopted to reduce computation time of subspace images deconvolution. Meanwhile, the performance of the proposed method may be further promoted by employing more effective

Fig. 13. Comparison results on images Barbara and Cameraman. Column 1: blur images and kernels. Columns 2 and 3: Zhong and proposed. Columns 4 and 5: absolute errors of Zhong and proposed.

Table 1
PSNR and ISNR variance of different methods in noise variation.

	TwIST [13]	L0GP [22]	FTVd [15]	JSM [25]	HLP [19]	Zhong [27]
PSNR Variance	14.34	0.20	24.73	14.60	18.53	0.02
ISNR Variance	14.31	0.20	24.71	14.57	18.49	0.02
	Proposed TwIST	Proposed L0GP	Proposed FTVd	Proposed JSM	Proposed HLP	Proposed Zhong
PSNR Variance	14.82	8.21	18.00	4.45	18.67	5.34
ISNR Variance	14.89	7.87	18.01	4.43	18.53	5.43

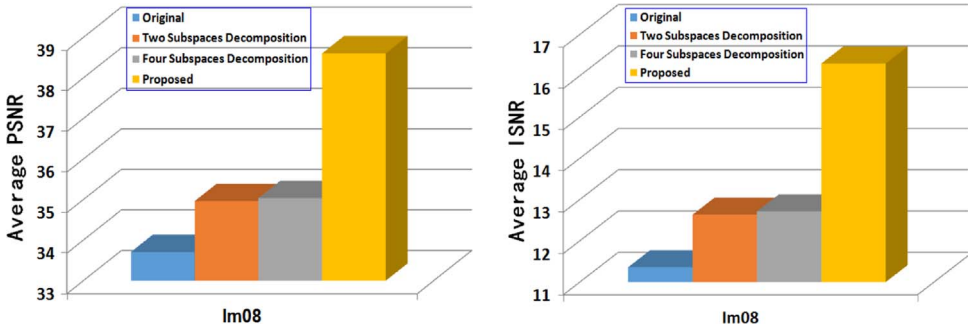

Fig. 14. Comparison of FTVd [15] with different ways of subspaces decomposition.

Fig. 15. Comparison of the proposed framework with different integration methods.

Table 2
Average time consumption comparison of different methods on Google image dataset (unit: seconds).

	TwIST [13]	L0GP [22]	FTVd [15]	JSM [25]	HLP [19]
Average	11.98	1.12	0.43	16.41	0.24
	Proposed TwIST	Proposed L0GP	Proposed FTVd	Proposed JSM	Proposed HLP
Average	22.62	3.31	1.11	49.18	0.71

models for different subspace images. These works will be explored in the near future.

Acknowledgments

This work was supported in part by the National Natural Science Foundation of China under Grants 61571382, 61571005, 81301278, 61172179, and 61103121, in part by the Guangdong Natural Science Foundation under Grant 2015A030313007, in part by the Fundamental Research Funds for the Central Universities under Grant 20720160075, 20720150169 and 20720150093, and in part by the Research Fund for the Doctoral Program of Higher Education under Grant 20120121120043.

Appendix A. Appendix

The filters of low-pass and high-pass are defined as follows: $l_1 = [0.5, 0.5]$, $l_2 = [0.5; 0.5]$, $g_1 = [-0.5, 0.5]$, and $g_2 = [-0.5; 0.5]$. Based on the definition of the filters, we formulate important properties of the filters in the Fourier domain as follows:

$$L_1^* \odot L_1 + G_1^* \odot G_1 = \mathbf{1} \tag{13}$$

$$L_2^* \odot L_2 + G_2^* \odot G_2 = \mathbf{1} \tag{14}$$

$$L_2 \odot L_1 + G_1 + G_2 \odot L_1 = \mathbf{1} \tag{15}$$

where L_1, G_1, L_2 and G_2 are the Fourier transform of l_1, g_1, l_2 and g_2, respectively. L_1^*, G_1^*, L_2^*, and G_2^* are the complex conjugate of L_1, G_1, L_2 and G_2, respectively. $\mathbf{1}$ is a matrix in which every element is equal to one. Due to the definition of the filters, the formula (10) is rewritten as

$$\begin{cases} h_1 = l_2 \otimes l_1 \\ h_2 = g_1 \\ h_3 = g_2 \otimes l_1 \end{cases} \tag{16}$$

and the Fourier form of the formula (16) is expressed as

$$\begin{cases} H_1 = L_2 \odot L_1 \\ H_2 = G_1 \\ H_3 = G_2 \odot L_1 \end{cases} \tag{17}$$

Based on the formulations (13), (14) and (17), the completeness of the filters $\{H_i\}_{i=1}^3$ is derived as follows:

$$\begin{aligned} \sum_{i=1}^{3} H_i^* \odot H_i &= H_1^* \odot H_1 + H_2^* \odot H_2 + H_3^* \odot H_3 \\ &\overset{(17)}{=} (L_2 \odot L_1)^* \odot (L_2 \odot L_1) + G_1^* \odot G_1 \\ &\quad + (G_2 \odot L_1)^* \odot (G_2 \odot L_1) \\ &= L_1^* \odot L_2^* \odot L_2 \odot L_1 + G_1^* \odot G_1 + L_1^* \odot G_2^* \odot G_2 \odot L_1 \\ &= L_1^* \odot (L_2^* \odot L_2 + G_2^* \odot G_2) \odot L_1 + G_1^* \odot G_1 \\ &\overset{(14)}{=} L_1^* \odot L_1 + G_1^* \odot G_1 \overset{(13)}{=} \mathbf{1} \end{aligned} \tag{18}$$

Meanwhile, based on the formulations (5), (15) and (17), the original image is reconstructed by three subspace images in the Fourier domain as follows:

$$\begin{aligned} \sum_{i=1}^{3} X_i = X_1 + X_2 + X_3 &\overset{(5)}{=} H_1 \odot X + H_2 \odot X + H_3 \odot X \\ &\overset{(17)}{=} L_2 \odot L_1 \odot X + G_1 \odot X + G_2 \odot L_1 \odot X \\ &\overset{(15)}{=} (L_2 \odot L_1 + G_1 + G_2 \odot L_1) \odot X = X \end{aligned} \tag{19}$$

Therefore, once the above three subspace images are obtained, the original image can be reconstructed in the Fourier and spatial domains as follows:

$$X_1 + X_2 + X_3 = X \Leftrightarrow x_1 + x_2 + x_3 = x \tag{20}$$

where $\Leftrightarrow$ denotes the equivalent operation.

References

[1] R. Fergus, B. Singh, A. Hertzmann, S.T. Roweis, W.T. Freeman, Removing camera shake from a single photograph, ACM Trans. Graph 25 (3) (2006) 787–794.
[2] A. Levin, R. Fergus, F. Durand, W.T. Freeman, Image and depth from a conventional camera with a coded aperture, ACM Trans. Graph 26 (3) (2007) 70.
[3] L. Yuan, J. Sun, L. Quan, H. Shum, Progressive inter-scale and intra-scale non-blind image deconvolution, ACM Trans. Graph 27 (3) (2008) 74.
[4] L. Xu, S. Zheng, J. Jia, Unnatural L0 sparse representation for natural image deblurring, in: IEEE International Conference on Computer Vision and Pattern Recognition (CVPR), June 2013, pp. 1107–1114.
[5] L. Sun, S. Cho, J. Wang, J. Hays, Good image priors for non-blind deconvolution: generic vs specific, in: European Conference on Computer Vision (ECCV), September 2014, pp. 31–246.
[6] A. Tikhonov, On the stability of inverse problems, Dokl. Akad. Nauk SSSR 39 (5) (1943) 195–198.
[7] L.B. Lucy, An iterative technique for the rectification of observed distributions, Astron. J. 79 (1974) 745–754.
[8] W. Richardson, Bayesian-based iterative method of image restoration, J. Opt. Soc. Am. 62 (1) (1972) 55–59.
[9] S. Osher, L. Rudin, E. Fatemi, Nonlinear total variation based noise removal algorithms, Physica D 60 (1992) 259–268.
[10] L. Rudin, S. Osher, Total variation based image restoration with free local constraints, in: IEEE International Conference on Image Processing (ICIP), 1994, pp. 31–35.
[11] A. Chambolle, An algorithm for total variation minimization and applications, J. Math. Imaging Vis. 20 (1–2) (2004) 89–97.
[12] T. Chan, S. Esedoglu, F. Park, A. Yip, Recent developments in total variation image restoration, Math. Models Comput. Vis. 17 (2005).
[13] J.M. Bioucas-Dias, M.A.T. Figueiredo, A. New TwIST, Two-step iterative shrinkage/thresholding algorithms for image restoration, IEEE Trans. Image Process 16 (12) (2007) 2992–3004.
[14] I. Daubechies, M. Defriese, C. De Mol, An iterative thresholding algorithm for linear inverse problems with a sparsity constraint, Comm. Pure Appl. Math. LVII (2004) 1413–1457.
[15] Y. Wang, J. Yang, W. Yin, Y. Zhang, A new alternating minimization algorithm for total variation image reconstruction, SIAM J. Imaging Sci. 1 (3) (2008) 248–272.
[16] C.R. Vogel, M.E. Oman, Iterative methods for total variation denoising, SIAM J. Sci. Comput. 17 (1) (1996) 227–238.
[17] A. Beck, M. Teboulle, Fast gradient-based algorithms for constrained total variation image denoising and deblurring problems, IEEE Trans. Image Process 18 (11) (2009) 2419–2434.
[18] A. Beck, M. Teboulle, A fast iterative shrinkage-thresholding algorithm for linear inverse problems, SIAM J. Imaging Sci. 2 (1) (2009) 183–202.
[19] D. Krishnan, R. Fergus, Fast image deconvolution using hyper-Laplacian priors, in: Advances in Neural Information Processing Systems (NIPS), 2009, pp. 1033–1041.
[20] D. Krishnan, T. Tay, R. Fergus, Blind deconvolution using a normalized sparsity measure, in: IEEE International Conference on Computer Vision and Pattern Recognition (CVPR), June 2011, pp. 2657–2664.
[21] L. Xu, C. Lu, Y. Xu, J. Jia, Image smoothing via L0 gradient minimization, ACM Trans. Graph 30 (6) (2011) 174.
[22] J. Pan, Z. Hu, Z. Su, M. Yang, Deblurring text images via l0-regularized intensity and gradient prior, in: IEEE International Conference on Computer Vision and Pattern Recognition (CVPR), June 2014, pp. 2901–2908.
[23] W. Dong, L. Zhang, G. Shi, Centralized sparse representation for image restoration, in: IEEE International Conference on Computer Vision (ICCV), November 2011, pp. 1259–1266.
[24] W. Dong, L. Zhang, G. Shi, X. Li, Nonlocal centralized sparse representation for image restoration, IEEE Trans. Image Process 22 (4) (2013) 1620–1630.
[25] J. Zhang, D. Zhao, R. Xiong, S. Ma, W. Gao, Image restoration using joint statistical modeling in a space-transform domain, IEEE Trans. Circuits Syst. 24 (6) (2014) 915–928.
[26] Y. Tai, S. Lin, Motion-aware noise filtering for deblurring of noisy and blurry images, in: IEEE International Conference on Computer Vision and Pattern Recognition (CVPR), June 2012, pp. 17–24.
[27] L. Zhong, S. Cho, D. Mextaxas, S. Paris, J. Wang, Handling noise in single image deblurring using directional filters, in: IEEE International Conference on Computer Vision and Pattern Recognition (CVPR), June 2013, pp. 612–619.
[28] R.C. Gonzalez, R.E. Woods, Digital Image Processing, Prentice-Hall, New Jersey, 2001.
[29] V.M. Patel, R. Maleh, A.C. Gilbert, R. Chellappa, Gradient-based image recovery methods from incomplete fourier measurements, IEEE Trans. Image Process 21 (1) (2012) 94–105.
[30] L. Xu, J. Jia, Two-phase kernel estimation for robust motion deblurring, in: European Conference on Computer Vision (ECCV), September 2010, pp. 157–170.
[31] M.S. Almeida, L.B. Almeida, Blind and semi-blind deblurring of natural images, IEEE Trans. Image Process 19 (1) (2010) 36–52.
[32] A. Levin, Y. Weiss, F. Durand, W.T. Freeman. Understanding and evaluating blind deconvolution algorithms, IEEE International Conference on Computer Vision and Pattern Recognition (CVPR), 2009, pp. 1964–1971.
[33] H. Zhang, J. Yang, Scale adaptive blind deblurring, in: Advances in Neural Information Processing Systems (NIPS), December 2014, pp. 3005–3013.